# EVALUATION OF FIBRE OPTIC SENSING TECHNIQUES FOR HELICOPTER ROTOR BLADES DURING GROUND RUN AND WHIRL TOWER TEST

Simone Weber[1]

Valerio Camerini[2], Raphael Rammer[1], Florian Kurfiss[1], Benedikt Köhr[1], Maxime Asselin[2], Kevin Mullaney[3], Thomas Kissinger[3,4], Stephen W James[3], Ralph P Tatam[3]

1) Airbus Helicopters Deutschland GmbH, Donauwörth, Germany
2) Airbus Helicopters S.A.S., Marseille Provence International Airport, France
3) Engineering Photonics, Cranfield University, Bedford MK43 0AL, United Kingdom
4) Now: TU Ilmenau, Institute of Process Measurement and Sensor Technology, 98693 Ilmenau, Germany.

**Abstract**

Optical fibre strain and shape measurement sensors were deployed on two bearingless main rotor systems, Airbus Helicopters H135 and Airbus Helicopters H145 (or BK117 D-3) during ground runs with controlled pilot inputs and during a whirl tower test. The sensing capabilities of two optical fibre-based strain sensing techniques, optical fibre Bragg grating (FBG) and fibre segment interferometry (FSI), and direct fibre optic shape sensing (DFOSS), a shape measurement based on the FSI approach, were benchmarked against conventional strain gauge measurements. Signal-to-noise ratios and modal properties were determined from the collected strain and displacement signatures using an improved operational modal analysis suitable for the removal of amplitude-modulated rotor harmonics and large rotor speed variations. It was shown not only that all fibre-optic based sensing techniques provide detailed understanding into the dynamic properties of the blade, but the measurements also offer insights into couplings from the airframe to the rotor and couplings from the drive train to the rotor. Results and discussions of the analysis of the measurements from the DFOSS system highlight its benefits over strain gauges or of the FBG strain sensing approach.

## 1. NOTATION

**Symbols**

| | |
|---|---|
| $\mathbf{A}$ | State matrix |
| $\mathbf{C}$ | Observation matrix |
| $f$ | Frequency |
| $f_{max}(t)$ | Frequency maximum |
| $n$ | Discrete sample of a signal |
| $o(n)$ | Order |
| $s_i$ | Actuator stroke characteristics |
| $SNR_H$ | Signal to noise ratio of the rotor excitation w.r.t. the residual signal |
| $t$ | Time |
| $\mathbf{v}_k$ | Measurement noise vector |
| $\mathbf{w}_k$ | Process vector |
| $x(n)$ | Measured signal |
| $x(t)$ | Acceleration signal |

| | |
|---|---|
| $\mathbf{x}_k$ | State vector |
| $x_{\Delta f}(t)$ | Filtered signal |
| $x^i_{\Delta f}(t)$ | Hilber transform of filtered signal |
| $X(t, f)$ | Magnitude of the short time Fourier transform |
| $\mathbf{y}_k$ | System response |
| $z_{\Delta f}(t)$ | Analytical signal |
| $\gamma(\tau)$ | Analysis window function |
| $\delta f$ | Frequency tolerance for maxima detection |
| $\Delta f$ | Frequency tolerance |
| $\Delta f_0$ | Initial frequency band |
| $\Delta f_t$ | Frequency set |
| $\Delta t$ | Sampling interval |
| $\Delta\zeta$ | Damping tolerance |
| $\epsilon(n)$ | Non-homogeneity term |
| $\eta(n)$ | Nuisance component |
| $\theta(n)$ | Instantaneous phase |
| $\theta_0$, $\theta_{1c}$, $\theta_{1s}$ | Multi-blade frame, control angles |
| $\theta_i$ | Blade coordinate for excitation signal |
| $\varphi_i$ | Azimuth angle, blade coordinates |
| $\varphi_f(t)$ | Instantaneous phase |
| $\phi$ | Displacement mode shape |
| $\Psi_i$ | Azimuth angle, hydraulic actuators |
| $\psi$ | Strain mode shape |

**Acronyms**

| | |
|---|---|
| AIM | Advanced In-Flight Measurement |
| DFOSS | Direct fibre optic shape sensing |
| EMA | Experimental modal analysis |
| FBG | Fibre Bragg grating |
| FE | Finite element |
| FSI | Fibre segment interferometry |
| MAC | Modal assurance criterion |
| OFS | Optical fibre sensor |
| OMA | Operational modal analysis |
| PSD | Power spectral density |
| SG | Strain gauge |
| SSI | Stochastic subspace identification |
| STFT | Short time Fourier transform |
| TSA | Time synchronous average |
| VKF | Vold-Kalman filter |
| WTT | Whirl tower test |

## 2. INTRODUCTION

Electrical strain gauges (SG) have been used for the measurement of aircraft structural loads for more than 70 years [1-5]. However, methods using SG have numerous disadvantages. These range from operational limitations, such as high sensitivity and the adverse influence of precipitation, to long installation times due to tedious wiring of each sensor. Moreover, for long and slender structures like rotor blades, the large amount of wiring interferes with the aerodynamic and dynamic behaviour of the blade and it is not uncommon that SGs fail during the testing. Robust and reliable measurement of rotating blade deformation is challenging and the search for new non-intrusive measurement techniques has been the subject of numerous studies. While imaging approaches have been trialled in wind tunnels and on whirl rigs [6], their in-flight use is hampered by the large observation angle and depth of field required to measure along the entire length of the blade, along with issues related to background light and to the fouling of the blade surface. Optical fibre-based approaches have the potential to meet both the measurement requirements and the demands of the measurement environment. Moreover, the deployment of optical fibre sensors (OFS) on helicopter rotor blades can provide data of the in-service strain and operational mode shapes. This could have significant impact from a number of engineering perspectives, ranging from the validation of the aeroelastic models underpinning numerical approaches to rotor design and manufacturing, to increasing the accuracy of control load prediction, paving the way for condition-based maintenance. OFS could provide a viable solution to replace the electrical SG as they offer several advantages over conventional sensors, including their flexibility, low weight, electromagnetic immunity, small dimensions (diameter of order 0.2 mm), and the absence of a requirement for electrical connection to the sensor elements. While, to-date, the primary focus of the aerospace applications of OFS has been on fixed wing aircraft [7], with numerous demonstrations of their use for the monitoring of a range of aspects of aircraft systems, including aircraft balance, structural health, and landing gear [8], there have been limited reports of their deployment on rotorcraft components in laboratory conditions [9-12], and under flight, or flight-equivalent, conditions [13–18]. Recent work [9] has shown the possibility of local strain and temperature measurement of the rotor blade from the start of its curing cycle through to demoulding, demonstrating that the sensors are sufficiently robust to survive the manufacturing process. Other approaches [19] made use of a full span strain sensor embedded into a scaled rotor blade that allows the integration of strain over the length. It only requires the location of the elastic and neutral axes along the span to determine elastic deflections and twist information. As part of the BladeSense programme [14], we deployed optical fibre-based sensing techniques on the rotor blades of an Airbus Helicopters H135. Data from optical fibre Bragg grating (FBG) and fibre segment interferometry (FSI) based strain sensors, and from FSI-based direct fibre optic shape sensing (DFOSS) instrumentation were live-streaming during a series of ground runs with controlled pilot inputs. Aspects of the work and the findings have been presented previously [15-17], where it was shown that the fibre optic strain and shape sensing approaches were capable of detecting the 1/rev rotation frequency, and its harmonics, and of detecting some of the operational modes excited by specific pilot inputs. While the sensitivity and accuracy of the OFS measurements during the BladeSense programme still have to be validated and related to the dynamic properties of the H135 rotor blade, we have shown during a recent whirl tower test [20] that OFS are capable of capturing rotor blade dynamics of up to 50 Hz induced by hydraulic actuator inputs.

The identification of modal properties of rotating structures is challenging [21-24], yet it is important for a wide range of activities, including validation of structural and aeroelastic models, design improvement, and vibration control. In this case, classical experimental modal analysis (EMA) can be performed in the setting of a whirl tower test (WTT), as the system excitation is controllable. However, EMA presents some drawbacks, notably related to the difficulty of simulating the actual operational boundary conditions, leading at times to loss of representativity of the obtained modal models [21]. Additionally, the structure to be analysed has to be well known to be able to identify the modal properties through the EMA method as deployed in [20]. During actual operations, it is often not possible to measure the input excitations, and identification can rely solely on the measured responses. In these cases, operational modal analysis (OMA) is used to test a structure under real boundary conditions [25]. Most OMA methods are based on the assumption of broadband environmental excitation. Therefore, as explained in [22], the application of OMA to rotating structures requires careful removal of rotor harmonics and periodic aerodynamic effects, as these would hamper modal estimation during the identification process [23-24]. A wide range of techniques have been developed for the purpose of correctly identifying and removing harmonic loading [21,23,26].

In this work, the modal parameters are estimated using stochastic subspace identification (SSI) in the time domain for OMA. Prior to the application of SSI, an approach based on the Vold-Kalman filter (VKF) [27-28] was used to design a selective, adaptive filter capable of removing amplitude-modulated harmonics from the signals. This works well for signals where the modulation timescale is significantly slower than the fundamental period, as the method allows the tracking of the amplitude evolution of each considered harmonic in time. Differently from harmonic removal methods based on time synchronous average (TSA) [29-30], which rely on averaging the measured signal data in periods synchronous to the fundamental harmonics to be removed, the adopted Vold-Kalman-based approach accounts for amplitude modulation of the rotor harmonics (according to the conventions of rotating machinery analysis literature, individual frequency components relating to the rotor and its harmonics are referred to as “orders” in the following) that may have been induced by stochastic aerodynamic loads. Both these methods need accurate rotor speed measurements. In the absence of such measurements, a procedure for instantaneous angular speed estimation similar to that described in [31], was considered, with the goal of developing an analysis method robust to large rotor speed variation cases, such as those that can be encountered during run-ups or specific operations with variable-speed rotors, and at the same time independently from the availability of a precise tachometer reference. The proposed harmonic removal method is therefore robust to rotor speed variations and able to account for order amplitude variations. Such features are desirable for operational modal analysis of helicopter data and motivated its use here.

The work reported here evaluates fibre optic sensing techniques on rotating rotor blades with the use of an OMA approach capable of the removal of amplitude-modulated rotor harmonics and large rotor speed variations. A description will be given of the deployment of the different types of sensing solutions on a main rotor blade of an Airbus Helicopters H135 helicopter during ground runs (as part of the BladeSense project [14-17]) and of an Airbus Helicopters H145 (or BK117 D-3) rotor blade during a WTT (presented in [20]). The first part of the paper briefly describes an established in-house EMA method that is used to determine how to compare the performance of FBG strain sensors with conventionally deployed SGs during a WTT. This is followed by a detailed description of the proposed OMA method, including rotor harmonic identification and its filtering from the collected data set. EMA is not only used to assess the accuracy of FBG strain sensors against SG, it will act as a reference to verify the OMA approach before its use to analyse the BladeSense data. The final part of the paper is concerned with the application of the described method to the BladeSense data to determine the sensitivity and accuracy of the OFS measurements during track and balance runs and during a sequence of pilot inputs. A comparison between FBG, FSI and DFOSS will pinpoint which instrumentation system provides better signals for dynamic characterization. The outcome of this paper demonstrates the potential use of OFS for providing in-service operational data on helicopter blade dynamics.

## 3. INSTRUMENTATION

### 3.1. WTT: SG and FBG sensors

Three FBG sensor arrays were deployed on the flexbeam of the bearingless main rotor of an Airbus Helicopters H145, each containing 4 wavelength-division-multiplexed FBGs fabricated in Ormocer coated 125µm single mode optical fibres, with the sensors distributed along a 0.4m length of fibre. The FBG sensor arrays were bonded to the upper and lower surfaces of the flexbeam (see Figure 1) using adhesive AE10, while Gagekote #8 was applied on top of the optical fibres as a first protective layer. The entire length of each optical fibre cable was covered with Silicone 3140 RTV to prevent the fibres from detaching. Standard electrical SG instrumentation was deployed at 12 radial positions as a reference during the test campaign. It was ensured that the FBGs were located as close as possible to the SGs, despite the limited available space due to the required wiring of each single SG on the flexbeam structure. The SGs form a full bridge configuration, meaning they are arranged symmetrically around the neutral axes, similar to the set-up presented in Figure 1(b). The different sensor locations are depicted in Figure 1(a) showing the positions of the SGs and the fibre sensors that were deployed on the lower surface of the flexbeam, with FBGs G1a to G4a on the leading edge and G1b to G4b on the trailing edge. Figure 1(b) shows the deployment of a further four FBGs, two on the upper surface and two on the lower surface. Figure 1(c) is an image of the final instrumented flexbeam, highlighting the limited installation space for FBGs G1c to G4c.

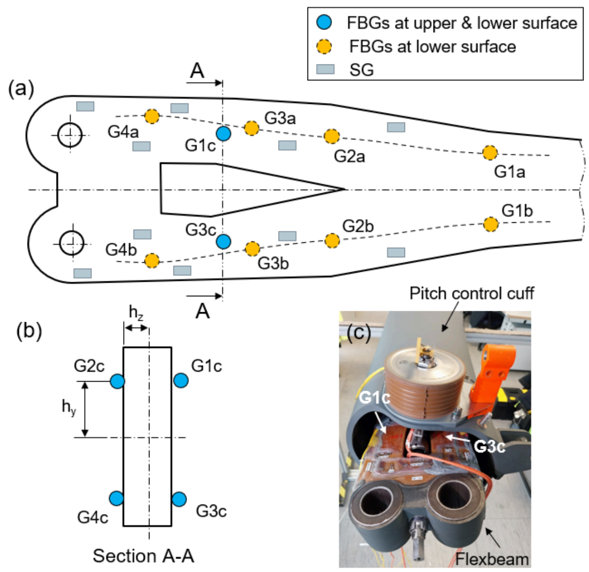


Figure 1: (a) Diagram showing positions of the SGs and the fibre sensors deployed on the lower surface of the flexbeam, with FBGs G1a to G4a on the leading edge and G1b to G4b on the trailing edge, (b) showing fibre sensors deployed on the upper and lower surfaces of the flexbeam with FBGs G1c to G4c, (c) image of the sensor positions G1c and G3c.

### 3.2. BladeSense: FBG and FSI sensors

The rotor blade was instrumented with OFS located along the leading edge. The sensor arrays covered approximately 55% of the rotor length and all fibre optic sensors were covered by the blade protection tape that is routinely applied in this area to protect the blade from minor impacts and erosion, such as sand, dirt or other debris. Four FBG sensor arrays, each containing 10 wavelength-division-multiplexed FBGs, were fabricated in-house at Cranfield University, in hydrogen loaded SMF 28 optical fibre with the sensors optimally distributed along a 2.1 m length of the fibre to ensure that the structural modes of interests could be captured with the number of sensors available. The positions of the sensors are shown in Figure 2. The arrays were interrogated using a commercial FBG interrogator, SmartScan Aero Mini.

The other two OFS technologies deployed on the rotor blade for the BladeSense ground runs rely on FSI [32], which is an optically and mechanically robust approach to the demodulation of the signals from an array of intrinsic interferometric strain sensors. Here the approach is used to measure both strain and shape. Arrays of 11 ultra short and low reflectively fibre Bragg gratings (LR-FBGs) were fabricated in-house at Cranfield University in eight lengths of hydrogen loaded SMF 28, with adjacent LR-FBGs separated by 190 mm. These fibre segments are arranged back-to-back, forming a continuous sensing chain. In FSI the spectral information of the FBG-based reflectors is not analysed, but instead, the reflectors merely serve as a means to define the fibre segment interferometers. Compared to regular electrical SGs and FBGs, the strain measurement in FSI is not localised, but is rather an integrated strain measurement over the length of each segment. The interferometric strain sensors were also used for DFOSS, achieved by using four optical fibres that were integrated within a flexible plastic rod specifically designed to facilitate DFOSS [16]. The fibres were bonded using cyanoacrylate into slots machined along the length of the rod, described in [16]. The rod itself was attached to the blade using cyanoacrylate adhesive. The locations of the FSI sensor elements in the span wise direction along the blade are shown in Figure 2, with reflectors, R1 to R11, and the corresponding segments, S1 to S10, formed between them, indicated. For DFOSS, appropriate processing of the differential strains experienced by the corresponding fibre segments in the four fibres allows the direct independent measurement of the slope angles in the vertical and horizontal directions [32]. Here, a cubic spline interpolation between reflector locations is then used to obtain a continuous slope angle curve, and subsequent spatial integration yields the vertical and horizontal displacement curves. A key benefit of this approach is the insensitivity to temperature, due to the differential nature of DFOSS measurement. Crucially, DFOSS allows direct determination of operational shapes of the blade from deformation data that is internally measured within the sensor cable. Therefore, full strain transfer from the blade to the sensor is not needed and there is no requirement for a model of the underlying structure. For more information on this technology the reader is referred to [10,15,16,32]. The FSI sensors were interrogated using an interrogator designed at Cranfield, and constructed to meet the certification requirements for the ground tests.

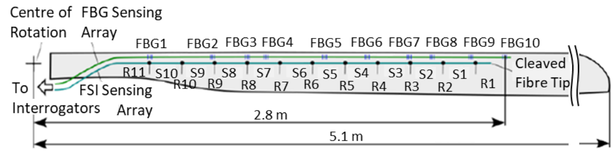


Figure 2: Diagram showing positions of the fibre sensors deployed on the lower surface of the rotor blade, with FBGs G1 to G10 and FSI sensing segments S1 to S10 shown. The black dots in the FSI sensor array represent the locations of the FSI reflectors, R1 to R11.

## 4. EXPERIMENTAL CONDITIONS

### 4.1. WTT

The WTT arrangement is presented in Figure 3. The FBG sensor arrays were interrogated using a commercial FBG interrogator, SmartScan Aero Mini, mounted on top of the rotor mast. The interrogator was run at a data rate of 2.5 kHz during the WTT campaign. A sampling rate of 0.5 kHz was used for the Airbus internal measurement and control system that allows the determination of bending moments from the SG measurements, calibrated to the flap (out-of-plane) and lead-lag (in-plane) moments.

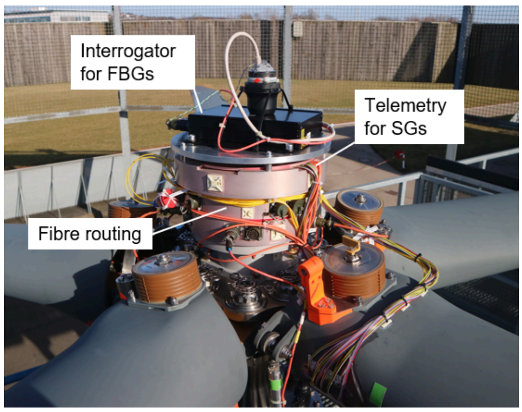


Figure 3: Whirl-tower test: Integration of FBG strain sensors and electrical SG with their dedicated data transfer devices on a H145 (BK117 D-3) rotor blade and rotor head.

In this case, the data transfer from the rotating to the fixed frame was achieved via an inductive Manner telemetry system connected to the ground station, while the FBG strain sensor data was streamed wirelessly. It was not possible to synchronise the data of the FBGs with the SGs by means of a precision time protocol during the test. Instead, the synchronisation had to be performed manually before the data analysis.

A WTT was carried out to identify the rotor loads and the modal properties of the main rotor blade, such as its natural frequencies and related damping in the flap and lead-lag directions [20]. In [20] it is explained how the rotor blade is excited in such a controlled environment with three hydraulic actuators that reproduce the collective and cyclic control inputs to the blade via the pitch links. Data was then collected during several track and balance runs and dedicated test runs with different excitation inputs for frequency and performance determination.

### 4.2. BladeSense

To investigate the performances of the deployed OFS technologies, ten ground runs of the helicopter were undertaken over three days. The assessment of each sensing technology involved the installation of a balanced hub support cap assembly, containing the optical system, power supply, PC, WiFi and fibre connectors, onto the mast (Figures 4 and 5). Two short track and balance runs to adjust and verify the balance of the blades were performed. A series of ground runs were then undertaken. When the rotor was operating at full speed, the pilot made discrete inputs to the collective and cyclic controls, with the set of inputs repeated three times during ground run.

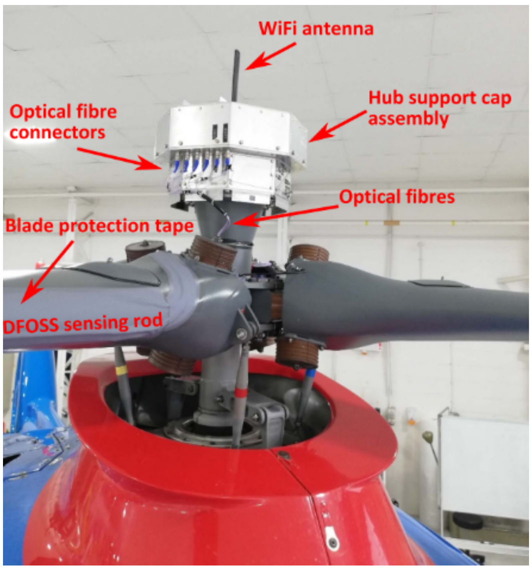


Figure 4: Hub support cap assembly mounted on the rotor mast.


Figure 5: BladeSense ground runs: H135 helicopter with hub support cap and instrumented blades during a ground run.

Four sets of pilot inputs were applied as indicated in Figure 6, stepped collective, doublet collective, doublet cyclic lateral and doublet cyclic longitudinal. The flight torque measurement was used as an indicator of the collective settings. For the cyclic control input, the stick position was moved in specific directions: backward and forward for cyclic longitudinal, and left and right for cyclic lateral input. To correctly perform the input, the stick positions were always moved to the neutral positions in between each input.

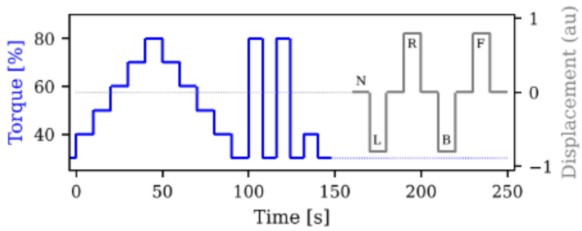


Figure 6: Planned pilot input pattern to the collective and cyclic controls; stepped collective (0–100 s), collective doublet (100–150s), cyclic (160–250 s), N—neutral, L—left, R—right, B—backward, F—forward.

## 5. METHODS

In this section, the methods used for modal identification are presented. For the laboratory WTT, it was possible to perform both classical EMA and OMA. For OMA analysis, the first step was to identify and remove from the measurements the harmonic loading originating from the rotor. Then, the residual signal was fed to the Stochastic Subspace Identification (SSI) in time domain algorithm in order to estimate the modal model of the structure under test. The choice of SSI for system identification was dictated by experience and by the availability of the implementation. However, a number of other techniques exist in the literature that could have been considered (see e.g. the review in [33]).

### 5.1. Experimental modal analysis

EMA involves the estimation of the input-output relationship between applied loads [34], i.e. the excitation signals from the hydraulic actuators, and the measured FBG and SG responses. To do so, the load signals were first transformed to the rotating frame, such that the measured strokes of the three actuators were transformed to multi-blade-coordinates using:

$$\theta_0 = s_1 + s_2 + s_3 \quad (1)$$

$$\theta_{1c} = -s_1 + s_2 cos(\Psi_2) + s_3 cos(\Psi_3) \quad (2)$$

$$\theta_{1s} = -s_2 cos(90 - \Psi_2) + s_3 cos(90 - \Psi_3) \quad (3)$$

Where $\theta_0$, $\theta_{1c}$ and $\theta_{1s}$ are the multi blade coordinates, and $\Psi_2$ and $\Psi_3$ are the fixed actuator azimuth position. The individual actuator stroke characteristics $s_1$, $s_2$, $s_3$ were transformed to pitch angle inputs. It should be noted that Eq. (1) is only valid for pure cyclic excitation schemes. These signals were then transformed to individual blade coordinates in the rotating frame by help of a rotor turn marker and rotor speed measurements available on the WTT to determine the azimuth angle $\varphi_i$ [35]:

$$\theta_i = \theta_0 + \theta_{1c} cos(\varphi_i) + \theta_{1s} sin(\varphi_i) \quad (4)$$

Where $\theta_i$ represents the excitation signal in the individual blade $i$ coordinates, and $\varphi_i$ the associated azimuth angle. Then, the transfer functions from input signal to each measurement signal were estimated through a dedicated Matlab function. The transfer function was approximated by a second order model by means of a nonlinear least-square solver, and the modal frequency and damping were identified from the system's parameters.

EMA results provide both a base of comparison for OMA methods in a laboratory setting, and a first assessment of the blades' modal properties under the WTT constraints.

### 5.2. Operational modal analysis

The operational modal analysis was performed in the time-domain, adopting SSI [36]. It is assumed that the system is linear and time-invariant, for which the stochastic state-space model is defined as:

$$\mathbf{x}_{k+1} = \mathbf{A}\mathbf{x}_k + \mathbf{w}_k \quad (5)$$

$$\mathbf{y}_k = \mathbf{C}\mathbf{x}_k + \mathbf{v}_k \quad (6)$$

Where $\mathbf{x}_k$ is the state vector with dimension $n \times 1$ (where $n$ is the system order to be determined), $\mathbf{y}_k$ is the system response of length $l \times 1$, $\mathbf{w}_k$ is the process vectors of length $n \times 1$ and and $\mathbf{v}_k$ is the measurement noise vector of length $l \times 1$. $\mathbf{A} \in \mathbb{R}^{n \times n}$ and $\mathbf{C} \in \mathbb{R}^{l \times n}$ are the state and observation matrices. For a detailed discussion on how to determine $\mathbf{A}$ and $\mathbf{C}$ the reader is referred to [36]. The essential quality of the algorithms within the subspace family is their ability to determine the matrices describing a linear system starting from subspaces containing the projections of data matrices. In particular, these algorithms project the space of the matrix rows of future outputs into the space of the rows of past outputs. Once the system matrices are estimated the modal parameters of the structural system can be computed from $\mathbf{A}$. To ensure that the modal properties can be clearly identified, a stabilisation diagram is used to determine stable poles and to neglect mathematical or spurious modes.

### 5.3. Harmonic identification and filtering

The objective of harmonic removal in OMA is to reduce the negative effect of the harmonic response at discrete frequencies on the modal identification process. In the literature, two main groups of techniques can be identified: the first [37] relies on filtering the harmonic components in the time series and using the residual for standard OMA; the second technique identifies the harmonic components together with the modal response [38]. In this work, harmonic identification is based on prior knowledge of the rotor frequencies, and therefore does not require automated harmonic load detection indices such as the Entropy Index proposed in [26]. In the general case, the rotor speed can change during the measurement period, either because the measurement is performed during the run-up phase or because the rotor speed varies following an acoustic or performance control law. In order to cope with varying rotor speed, it is necessary to have an estimation of the instantaneous rotor frequency. The latter could be measured with a tachometer or, lacking such measurement, estimated directly from the acceleration signal as proposed e.g. in [31].

Similarly to [31], the instantaneous frequency is estimated in this work based on the spectrogram of the acceleration signals. The spectrogram is defined as the squared magnitude of the short time Fourier transform (STFT) of the signal:

$$|X(t, f)|^2 \text{where } X(t, f) = \int_0^t x(t)\gamma(t - \tau)\, e^{-j2\pi f t}\, dt \quad (7)$$

In Eq. 7, $\gamma(\tau)$ is the analysis window function, $x(t)$ the acceleration signal as a function of time $t$, and $f$ is the frequency. Maxima tracking is then applied under the assumption that the rotor frequency is the most energetic component in the considered frequency band, so that:

$$f_{max}(t) = Argmax_f |X(t, f)|^2, \text{ for } f \in \Delta f_t \quad (8)$$

$$\Delta f_t \subset \left\{f_{max}(t - d\tau) - \delta f,\ f_{max}(t - d\tau) + \delta f\right\} \quad (9)$$

Where $\delta f$ is the frequency tolerance for maxima detection, and $X(t, f)$ is the STFT of signal $x(t)$ for the frequency values in the set $\Delta f_t$ specified from the previous estimate $f_{max}(t - d\tau)$. The initial band $\Delta f_0$ is specified by the user and represents the analysis band where the initial order frequency lies at the analysis time $t = 0$. The result is a coarse estimation of the instantaneous frequency as a function of time, $f_{max}(t)$. Based on that, the instantaneous phase can be computed by integrating the estimated frequency over time. Finally, the coarse phase is used to resample the signal in the angular domain using computed order tracking [39]. Then, the angular-domain signal is filtered around the order of interest and resampled back to the time domain using the coarse phase information, obtaining the filtered signal $x_{\Delta f}$. The instantaneous phase is then obtained from the analytical signal $z_{\Delta f}$:

$$z_{\Delta f}(t) = x_{\Delta f}(t) + j x^i_{\Delta f}(t) \quad (10)$$

as:

$$\varphi_f(t) = \text{imag}(\log(z_{\Delta f}(t))), \quad (11)$$

where $x^i_{\Delta f}(t)$ is the Hilber transform of $x_{\Delta f}(t)$.

The instantaneous phase and its multiples up to order $N$ are used in the second-generation VKF formulation [40] to extract the $N$ orders of interest from the signal. The VKF requires two equations: the structural equation and the data equation. The structural equation describes the mathematical characteristics of the order to be extracted, enforcing smoothness of the envelope. The data equation describes the relationship between the order $o(t)$ and the measured data $x(t)$ accounting for random noise and other components in the data. Second-generation, 2-poles VKF is used, which provides a good selectivity with respect to the single-pole, while being less computationally intensive than the 3-poles approach. The second-generation formulation results in the estimation of the envelope of a mono-component signal with a given instantaneous frequency or phase. The structural and data equations for the second-generation, 2-poles VKF (considering the case of a single extracted order) read:

$$\nabla^2 o(n) = o(n) - 2o(n + 1) + o(n + 2) = \epsilon(n), \quad (12)$$

$$x(n) = o(n) exp(j\theta(n)) + \eta(n), \quad (13)$$

Where the notation $x(n)$ corresponds to the discrete sample $n$ of the signal $x(t)$ such that $t = n\Delta t$, with $\Delta t$ being the sampling interval, $\epsilon(n)$ is a non-homogeneity term accounting for amplitude and frequency variations from a perfect sine wave model, $\theta(n)$ is the instantaneous phase and $\eta(n)$ is the nuisance component accounting for exogenous energy in the filter band.

Ultimately, the mono-component signals extracted with the VKF represent the harmonic excitation due to the rotor for the considered $N$ orders and can be subtracted from the original signal $x(t)$ in order to obtain the residual $x_r(t)$.

### 5.4. Signal-to-noise ratio evaluation

As part of the comparison between FBG and SG sensors, an analysis of their respective measurement noise is performed. For the considered data, the following metric is proposed for noise evaluation:

$$SNR_H = \frac{RMS(x_S(t))}{RMS(x_R(t))}, \quad (14)$$

which indicates the ratio of the RMS energy of the sum of the harmonic signals generated by the rotor,

$x_S$(t), to the energy of the residual signal $x_R(t)$ after harmonic removal as per Section 5.3. Such an index works well when the synchronous rotor excitation is similarly present in the compared sensors and has the advantage of not requiring particular considerations about band selection for noise floor estimation. It has, however, the drawback of being poorly representative when sensor placement makes the harmonic excitation significantly different between the compared sensors.

## 6. RESULTS AND DISCUSSION

### 6.1. Experimental modal analysis

In this section, EMA results obtained from the WTT data are presented, which use the input-output relationship during a sine-sweep excitation. While the outcome will give an insight into the performance of the FBG strain sensors compared to SG, it will also be used as reference to verify the OMA approach before analysing the BladeSense data.

#### 6.1.1. WTT data

During the test campaign, data totalling around nine hours was collected. While all of the FBG sensors survived the test campaign, one of the SG measurements failed during the whirl tower test. The malfunctioning SG was located at one of the flap moment measurement positions, which was mounted in a radius range, where large strains occur. This behaviour can often be observed during whirl tower testing or in early flight test phases since the strains experienced at some locations along the flexbeam of a bearingless main rotor can commonly exceed the measurement range of commercially available SGs.

Data was analysed adopting the EMA as described in Section 5.1. The errors between the natural frequencies $\Delta f$ obtained with the FBG and SG sensors are listed in Table 1, demonstrating very good agreement, with a percentage error of less than 0.6%. In a previously published paper [20] it was further shown that the determined flap and lead-lag bending moments were comparable. The modal damping percentage error, $\Delta\zeta$, of about 80% was subject to the specific FBG sensor positions which were not ideal for identifying this particular mode.

Table 1: Natural frequency error, $\Delta f$, and damping ratio error, $\Delta\zeta$, of FBG measurements relative to the SG measurements, taken during whirl tower test campaign with dedicated excitation inputs.

| Mode | $\Delta f$ (%) | $\Delta\zeta$ (%) |
|---|---|---|
| 1st lead-lag | -0.2 | 1.8 |
| 1st flap | Not identified with SG or FBG | |
| 2nd flap | 0.6 | -79.9 |
| 3rd flap | 0.0 | -11.5 |
| 1st torsion | Not identified with FBG | |
| 2nd lead-lag | 0.0 | -11.1 |
| 4th flap | 0.2 | 0.0 |

### 6.2. Operational modal analysis

This section begins by first verifying the output-only modal analysis approach, OMA, against the EMA outcome (Section 6.1.1). This is followed by deriving the modal properties from the BladeSense data.

#### 6.2.1. WTT data

Before applying the proposed OMA approach to the BladeSense ground run data, the method is first verified by extracting modal properties from the WTT track and balance run data and compared to the results obtained from the previously applied EMA approach. For comparison reasons, an example of a stabilisation diagram without data manipulation is computed first, which is depicted in Figure 7. This was achieved with the stabilisation criteria set as 1% for frequencies, 5% for damping, and 0.98 for the Modal Assurance Criterion (MAC) [41]. Engineering judgement was applied to exclude unrealistically high damping values for the blade. The stabilisation diagrams have been evaluated for a system order ranging from 20 to 140. The stabilisation diagram was used to pick the results selecting the order showing a good compromise between complexity and residual value. Figure 7 depicts that most stable poles are found around the rotor harmonics, making it difficult to identify the structural modes of interest. A person, experienced with the specific design of the rotor under investigation and having clear expectations about its frequency placement, would be able to distinguish between the influence of the harmonics and the normal modes. However, a modal identification from scratch, e.g. evaluating test results without knowledge of expected system behaviour, would be very difficult and most probably lead to erroneous results.

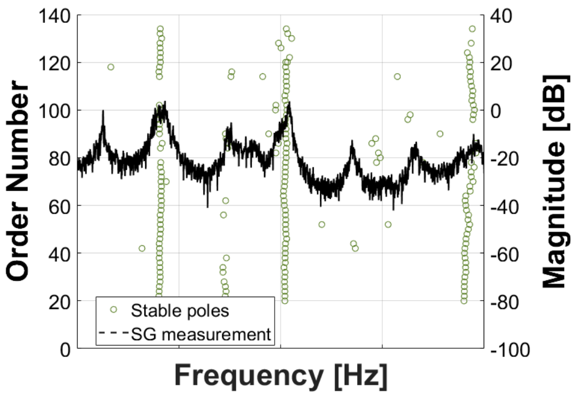


Figure 7: Stabilisation diagram for sensors in flap direction computed with the following parameters: $\Delta f = 1\%$, $\Delta\zeta = 5\%$, $\Delta MAC = 0.98$ for one realisation of SG measurements from the WTT track and balance run.

After applying the described approach, rotor harmonics were removed from the data set and an example of the stabilisation diagram with the harmonic content removed is presented in Figure 8. No peaks are present at the rotor harmonic frequencies, which allows a proper and straightforward identification of the blade modes. This significantly improves the evaluation of modal properties from an OMA approach.

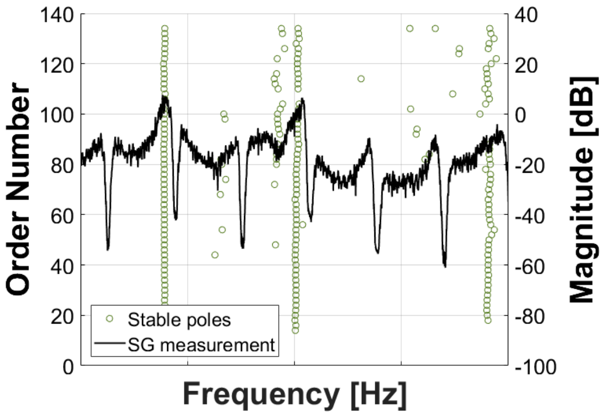


Figure 8: Stabilisation diagram for sensors in flap direction with removed amplitude-modulated rotor harmonics computed with the following parameters: $\Delta f = 1\%$, $\Delta\zeta = 5\%$, $\Delta MAC = 0.98$ for one realisation of SG measurements from the WTT track and balance run.

Table 2 lists the errors between the natural frequencies Δf obtained with FBG and SG sensors, comparing the EMA and OMA approaches. While OMA is an output-only modal analysis that was applied to one track and balance run, EMA uses the input-output relationship during a sine-sweep excitation. Since the operational condition of the rotor blade during the track and balance run is not representative of the same test conditions as analysed in [20], the damping is not compared.

Table 2: Natural frequency error, $\Delta f$, of OMA relative to EMA (presented previously in [20]) using data from the WTT track and balance run.

| Mode | ***OMA vs EMA SGs*** ***Δf*** **(%)** | ***OMA vs EMA FBGs*** ***Δf*** **(%)** |
|---|---|---|
| 1st lead-lag | 9.2 | Not identified with OMA |
| 1st flap | Not identified with SG or FBG | |
| 2nd flap | 1.2 | Not identified with OMA |
| 3rd flap | 7.8 | 1.4 |
| 1st torsion | Not identified with OMA | |
| 2nd lead-lag | Not identified with OMA | 0.1 |
| 4th flap | -0.1 | -0.6 |

All natural frequencies that could be identified from the SG data are in agreement with a percentage error of less than 9.2%. This particularly high deviation for the 1st lead-lag mode is expected due to the different test conditions. In the EMA tests, dedicated cyclic regressive excitation was performed. This leads to significantly larger lead-lag damper deflection amplitudes than those experienced during the track and balance runs that were exploited for the OMA evaluation. The shear stiffness of the elastomeric lead-lag dampers of the rotor blades is dependent on the deflection amplitude. An estimation of the difference between EMA and OMA tests leads to a factor of three difference in shear stiffness, which explains the deviation in the measured frequency. Due to the small number of FBGs on the flexbeam for the WTT, not all modes could be identified from the FBG data. All other modes exhibit a natural frequency error of less than 1.4%.

### 6.2.2. BladeSense data

After successfully verifying the OMA method, it was deployed on the BladeSense measurement data to validate the determined modal properties against WTT data on the same type of rotor blade that was collected previously as part of the AIM (Advanced In-Flight Measurement) project [42]. While 10 FBG and 10 FSI strain sensor positions were used for the SSI approach, 19 radial measurements were taken from the 100 radial positions provided by the DFOSS system. This still provides a good resolution measurement of the blade shape over the chosen sensing length. The natural frequency errors for the different modes obtained from the FBGs during the BladeSense ground runs and SG from the AIM WTT are listed in Table 3. As the data were derived under different operational conditions, namely a full scale helicopter ground run on high skids and a WTT, some deviations are expected, but the comparison still provides some understanding about the meaningfulness of the obtained results.

Table 3: Natural frequency error, $\Delta f$, of FBG relative to SG measurements taken during the AIM project [42], FSI and DFOSS system relative to FBG from BladeSense track and balance and dedicated ground runs.

| Mode | FBG vs SG (AIM WTT [41]) ***Δf*** **(%)** | FSI vs FBG ***Δf*** **(%)** | DFOSS vs FBG ***Δf*** **(%)** |
|---|---|---|---|
| 1st lead-lag | -7.7 | 8.8 | 5.1 |
| 1st flap | Not identified | | |
| 2nd flap | 3.1 | 0.7 | -3.2 |
| 3rd flap | -2.0 | 2.0 | 2.6 |
| 1st torsion | Not identified | | |
| 2nd lead-lag | 4.3 | -3.7 | -2.1 |
| 4th flap | -0.8 | -0.4 | -0.4 |

A maximum error of 7.7% for the 1st lead-lag mode was obtained, which is again influenced by the different test conditions. Otherwise, reasonable identification from the FBG data was achieved for the remaining modes, using the AIM WTT as a reference. Apart from identifying the blade's dynamic characteristics, more interesting information was found while analysing the BladeSense data, such as the observation that the dominant airframe mode coupled with the rotor blade dynamics on the ground, and the good visibility of the 2nd drive train mode evident in the blade behaviour. It is important to note that such observations should also be possible with SGs.

Furthermore, Table 3 also provides a comparison between FSI and FBG, as well as between DFOSS and FBG. It is noted that the DFOSS data, which contains separate data sets for horizontal and vertical deformations, proved to be easier to use than using the FSI strain data, as the flap and lead-lag modes are already decoupled within the DFOSS data set, providing information about the dominant mode directions. DFOSS data also provides an improved resolution of the deformation information along the rotor radius, compared to the FBG data. The DFOSS data allowed flapping and lead-lag rotor blade modes to be identified during the track and balance ground run. The evaluation of the FBG and FSI sensor data was more tedious and only worked out for modes with their main characteristics in the flap direction. FSI and FBG data from a ground run during which the pilot performed dedicated control input excitations were also used to obtain lead-lag characteristics. Using the OMA approach, the data time series were evaluated directly after quick control input change to obtain a near broadband excitation behaviour. For FSI, even the 2nd flap mode could be obtained from these test runs. Here collective and cyclic doublets proved to be the most effective pilot inputs, after which the lead-lag modes and the 2nd flap mode could be extracted. To obtain meaningful and confident modal results for FSI and FBG, the convergence settings for the creation of the stabilisation diagram had to be relaxed, and a limited set of sensors had to be chosen. For DFOSS data, all sensors could be used. It turned out that some prior knowledge about the structural system under investigation was necessary for the extraction of the modal data. Overall, a comparison of the FSI and corresponding DFOSS data against that from the FBG sensors revealed a maximum error of 8.8% for the 1st lead-lag mode, while the maximum frequency deviations of the remaining modes were within 4%. It should be noted that the natural frequency error obtained from the DFOSS and FSI deviate from each other. This could result from the influences of the centrifugal force, tension-torsion coupling and temperature, which were not compensated during FSI and FBG data evaluation, but which are inherently considered in the DFOSS approach.

Finally, both operational strain and displacement mode shapes were computed directly from the estimated state matrices determined using the output-only methodology SSI described in the previous section. The displacement and strain mode shapes were determined from a finite element (FE) beam model [43] and used for comparison and analysis. Figures 9 and 10 present a comparison of the 4th flap mode for the operational strain and displacement mode shapes, respectively.

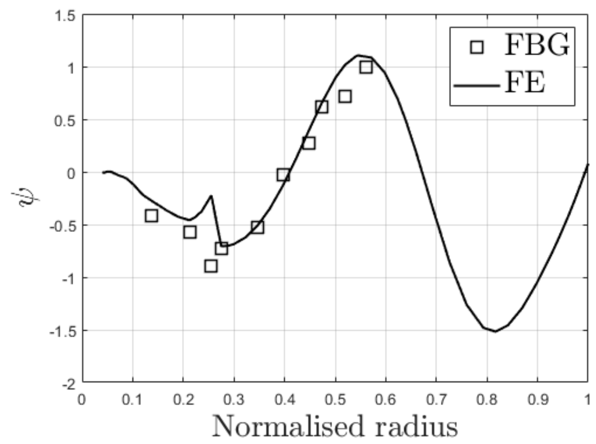


Figure 9: FBG strain mode shape ψ for 4th flap mode compared with FE beam models [43].

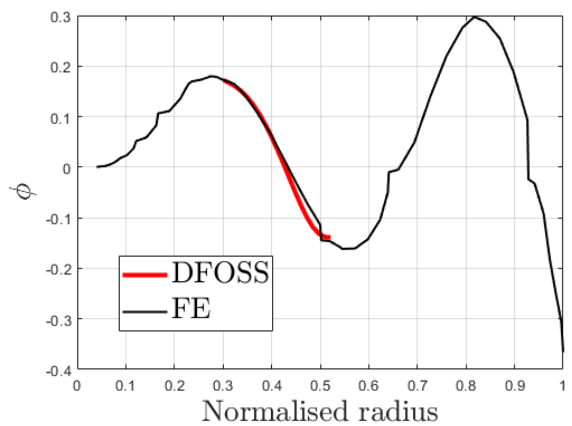


Figure 10: DFOSS displacement mode shape ϕ for 4th flap mode compared with FE beam models [43].

Table 4 reveals an excellent mode shape pairing for all modes identified from DFOSS data, while for FBG measurements lead-lag modes could not be identified and the mode shape correlation between measurement and calculation was poor for the 2nd and 3rd flap modes. Although it was demonstrated in [43] that the lead-lag modes will be difficult to predict with the chosen FBG sensor positions at the leading edge compared to having them installed on the trailing edge, it was decided during the project to install the sensors at the leading edge underneath the blade projection tape due to safety measures. Furthermore, the FBGs were located on a significantly stiffer structure than the flexbeam, resulting in lower strain signals than if the FBG sensors had been mounted on the flexbeam. Additionally, the outcome for the poor strain mode shape pairing could be also a result of numerical errors and a lack of detailed structural knowledge that highlighted difficulties in accurately predicting the surface strain from the FE beam model [43].

Table 4: Comparison of mode shape pairing with FE beam model using data from the BladeSense track and balance run.

| **Mode** | **MAC (FBG) (%)** | **MAC (DFOSS) (%)** |
|---|---|---|
| 1st lead-lag | Not identified | 99.97 |
| 1st flap | Not identified | |
| 2nd flap | 37.81 | 99.97 |
| 3rd flap | Poor MAC | 99.76 |
| 1st torsion | Not identified | |
| 2nd lead-lag | Not identified | 99.99 |
| 4th flap | 85.51 | 98.53 |

The achieved results clearly highlight the benefit of DFOSS over standard strain sensing for modal analysis, since two-dimensional deformation data is directly obtained with only one straight fibre rod, entirely independent of the location of the rod with respect to the neutral axis and without the requirement for strain transfer to the blade structure. Due to the differential nature of the measurement, temperature changes or effects due to centrifugal force do not lead to a DFOSS signal. This poses a major advantage of DFOSS as it is only sensitive to transversal motion and not longitudinal strain components along the sensor rod. Considering all these advantages, it not only suggests that further research in the application of DFOSS to mode shape analysis could be very fruitful, but also shows the great potential of directly determining the structural shape at any instance in time, as shown in a previous publication [16].

### 6.3. Signal-to-noise ratio evaluation

The signal-to-noise ratio was estimated for the considered datasets as detailed in Section 5.4.

#### 6.3.1. WTT data

The values of $SNR_H$ are presented in Figure 11 for each of the FBG and SG sensors, using the ratio of the synchronous signal obtained from the first five rotor harmonics to the residual signal filtered to the same frequency band. Signals from the track and balance run were considered, mostly consisting of rotor excitation.

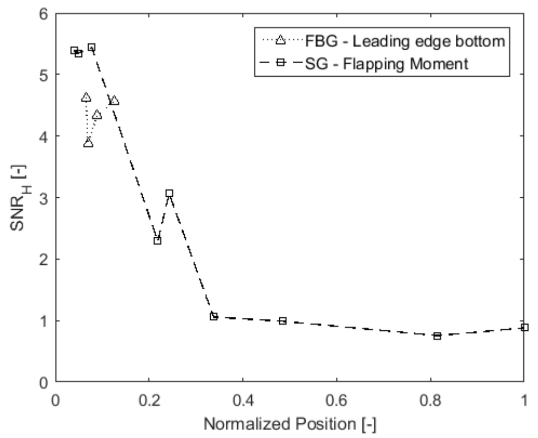


Figure 11: Comparison of signal-to-noise ratio $SNR_H$ for H145 WTT rotor track and balance data: triangles: FBG sensors, G1a - G4a, on bottom leading edge position; squares: SG sensors, flapping moment.

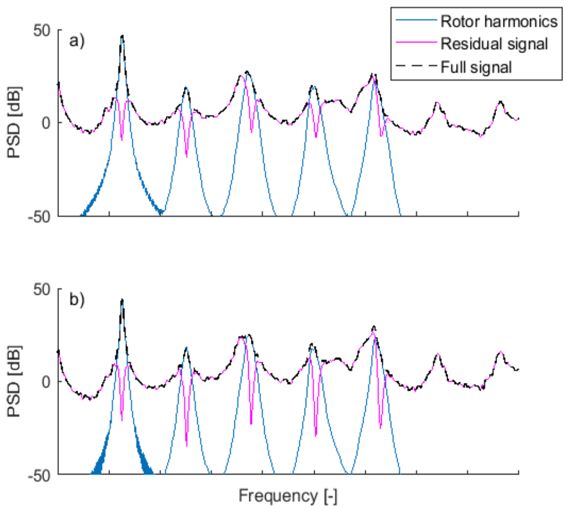


Figure 12: Comparison of full signal, residual signal and rotor excitation for H145 WTT rotor track and balance data: a) FBG sensor G2a, b) SG sensor MB320.

From Figure 11, it can be seen that the FBG and SG instruments yield a comparable SNR for most of the sensors. The values show a dependency on the sensor's radial position on the blade, according to the fact that higher strain is experienced close to the root, yielding therefore higher signal values with respect to the residual noise. Figure 12 demonstrates that, for both FBG and SG, the rotor excitation is effectively identified and removed from the signal.

#### 6.3.2. BladeSense data

Signal to noise ratio values for the FBG, FSI and DFOSS sensors are depicted in Figure 13 for the BladeSense rotor track and balance dataset.

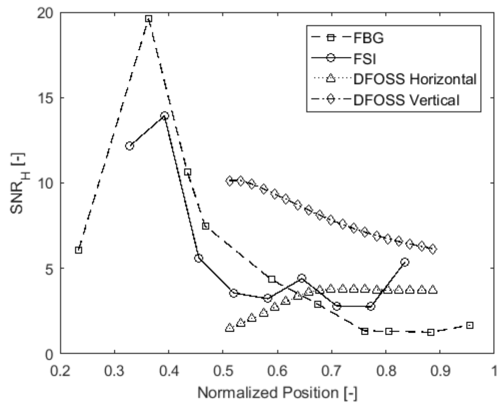


Figure 13: Comparison of signal-to-noise ratio $SNR_H$ of FBG, DFOSS and FSI sensors for BladeSense rotor track and balance data.

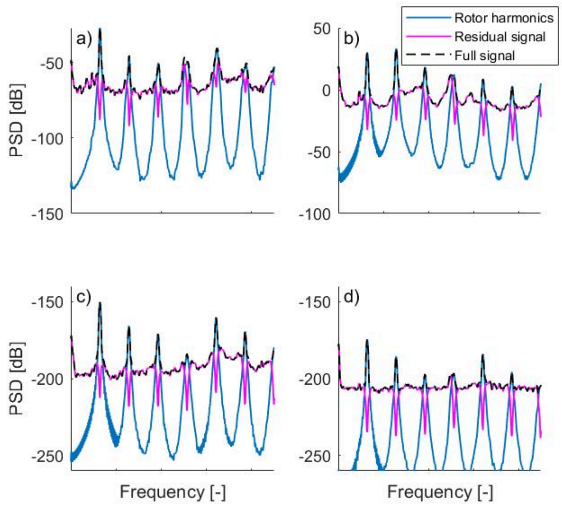


Figure 14: Comparison of full signal, residual signal and rotor excitation for BladeSense rotor track and balance data: a) FBG sensor FBG1, b) FSI sensor S1, c) DFOSS sensor vertical, d) DFOSS sensor horizontal.

The SNR of the vertical component from the DFOSS data is higher than that of the horizontal component due to the predominant flapping movement of the rotor blade. The DFOSS vertical component measurement shows higher SNR than FBG and FSI measurements for similar radial positions. Also, for this dataset, the harmonic separation allows correct identification and removal of the rotor excitation from the full signal, as shown in Figure 14.

## 7. CONCLUSIONS

Optical fibre strain and shape measurement sensors were deployed on two bearingless main rotor systems, Airbus Helicopters H135 and Airbus Helicopters H145 (or BK117 D-3), during ground runs and WTT. Data was streamed wirelessly from the rotor hub-mounted optical fibre sensor interrogators to a ground station. The strain sensing capabilities of three optical fibre-based sensing techniques, optical FBG and FSI strain sensors, and the shape measurement approach DFOSS, have been compared and assessed against conventional SG measurements with the aim to evaluate the measurement performances of the fibre optic sensing techniques deployed on rotating rotor blades. Signal-to-noise ratio and modal properties are compared by performing an improved operational modal analysis suitable for the removal of amplitude-modulated rotor harmonics and of the influence of large rotor speed variations. Additionally, the applied approach is verified against a standard in-house experimental modal analysis method.

During the WTT campaign, data totalling around nine hours was collected. While all of the FBG sensors survived the test campaign, one of the SG measurements failed during a whirl tower run with higher flexbeam loading. This behaviour of SGs on the flexbeams of bearingless main rotors has been established in previous studies, revealing that SGs are loaded at or above their fatigue limit during whirl tower and subsequent flight testing. Analysis of FBGs measurements during controlled WTT revealed very good performance, comparable to that of SG, with a natural frequency error of less than 0.6%. With regards to SNR, the FBG and SG yield a comparable SNR for most of the sensors.

The performances of all fibre optic-based sensing systems deployed during the BladeSense project were assessed with measurements collected during several ground runs, showing an agreement of better than 9% for the natural frequencies and a mode shape pairing of better than 98% for DFOSS. The mode shape pairing with FBG and the FE beam model was only sufficiently good for the 4$^{th}$ flap mode, with a MAC of 85.5%. From the ground run data it was not only shown that all fibre-optic based sensing techniques provided detailed understanding into the dynamic properties of the blade, but that they also provided insights into couplings from the airframe to the rotor and couplings from the drive train to the rotor. It is expected that such phenomena can also be observed with the use of SG. From the different data sets it was found that all modes of interest could be identified using DFOSS from a single track and balance run, while for FBG and FSI additional data from the collective and cyclic doublet excitation inputs had to be included to also obtain both lead-lag modes and the 2$^{nd}$ flap mode. Furthermore, it was demonstrated that SNR values of the DFOSS vertical component measurement were higher than those of the FBG and FSI measurements for similar radial positions. Results and discussions around the analysis of the DFOSS system reveal additional benefits that out-perform FBG strain sensing approach. These include insensitivity to temperature, and the direct determination of operational shapes of the blade without the requirement for strain transfer from the blade to the sensor and without the requirement for a model of the underlying structure. The high sensitivity of DFOSS and the capability to obtain two-dimensional shape information makes this measurement approach particularly suitable to determine the dynamic characteristics of complex structures in operational conditions.

While key challenges remain in the area of interrogator miniaturisation, robust data transfer from the rotating to the fixed frame and accurate time synchronisation between all acquisition systems, the outcome of this work demonstrates the potential of the use of optical fibre sensors for flight testing and for the provision of in-service operational data on helicopter blade dynamics.

Author contact:

Simone Weber simone.weber@airbus.com,
Valerio Camerini valerio.camerini@airbus.com,
Raphael Rammer raphael.rammer@airbus.com,

Florian Kurfiss florian.kurfiss@airbus.com,
Benedikt Köhr benedikt.koehr@airbus.com,
Maxime Asselin maxime.asselin@airbus.com,
Kevin Mullaney k.mullaney@cranfield.ac.uk,
Thomas Kissinger thomas.kissinger@tu-ilmenau.de,
Stephen W James s.w.james@cranfield.ac.uk,
Ralph P Tatam r.p.tatam@cranfield.ac.uk.

## 8. ACKNOWLEDGMENTS

The authors are grateful for valuable input and the support of the instrumentation development from colleagues from Cranfield University: Edmond Chehura, Huseyin Pekmezci, James Barrington, Stephen Staines, Thomas Charrett, Nicholas Lawson, and Mudassir Lone. Additionally, the authors would like to acknowledge the support of Sezsy Yusuf, for her invaluable advice on the deployment of the Stochastic Subspace Identification algorithm. The authors acknowledge support from Innovate UK via the Aerospace Technology Institute under ATI (102381), and from the Engineering and Physical Sciences Research Council (UK) (EP/N002520 and EP/V020218/1).

## 9. REFERENCES

1. Skopinski, T. H, Aiken, W. S. J., Huston, W. B., “Calibration of strain-gage installations in aircraft structures for the measurement of flight loads,” NACA Report 1178, 1954.
2. Kottkamp, E., Wilhelm, H., Kohl, D., “Strain gauge measurements on aircraft,” AGARD Flight Test Instrumentation Series, Vol. 7, (160), 1976.
3. Golub, R., McLachlan, W., “In-flight measurement of rotor blade airloads, bending moments, and motions, together with rotor shaft loads and fuselage vibration, on a tandem rotor helicopter,” Volume I. Instrumentation and in-flight recording system. Technical Report 67-9A, U.S. Army Aviation Materiel Laboratories, Virginia, USA, 1967.
4. Grant, W. J., Pruyn, R. R., “In-flight measurement of rotor blade airloads, bending moments, and motions, together with rotor shaft loads and fuselage vibration, on a tandem rotor helicopter,” Volume II. Calibrations and instrumented component testing. Technical Report 67-9B, U.S. Army Aviation Materiel Laboratories, Virginia, USA, 1967.
5. Riley, J., Padfield, G. D., Smith, J., “Estimation of rotor blade incidence and blade deformation from the measurement of pressures and strains in flight,” 14th European Rotorcraft Forum, Milano, Italy, 1988.
6. Boden, F., Stasicki, B., Ludwikowski, K., “Optical Rotor-Blade Deformation Measurements using a Rotating Camera,” The European Test and Telemetry Conference, 2018, pp. 147–154. DOI:10.5162/ettc2018/7.4.
7. Lawson, N. J., Correia, R. N. G., James, S. W., Partridge, M., Staines, S. E., Gautrey, J. E., Garry, K. P., Holt, J. C., and Tatam, R. P., “Development and application of optical fibre strain and pressure sensors for in-flight measurements,” *Measurement science and Technology*, Vol. 27, (10), 104001, 2016.
8. Cutolo, A., Bernini, R., Berruti, G. M., Breglio, G., Bruno, F. A., Buontempo, S., Catalano, E., Consales, M., Coscetta, A., Cusano, A., Cutolo, M. A, Di Palma, P., Esposito, F., Fienga, F., Giordano, M., Lele, A., Ladicicco, A., Irace, A., Janneh, M., Laudati, A., Leone, M., Maresca, L., Marrazzo, V. R., Minardo, A., Pisco, M., Quero, G., Riccio, M., Srivastava, A., Vaiano, P., Zeni, L., Campopiano, S., “Innovative Photonic Sensors for Safety and Security, Part II: Aerospace and Submarine Applications,” *Sensors*, Vol. 23, (5), 2417, 2023.
9. Asselin, M., “Caractérisation thermomécanique de composites stratifiés et instrumentation par fibre optique à réseaux de Bragg,” Ph.D Thesis, 2023.
10. Weber, S., Kissinger, T., Chehura, E., Staines, S., Barrington, J. H., Mullaney, K., Fragonara, L. Z., Petrunin, I., James, S. W, Lone, M., and Tatam, R. P., “Application of fibre optic sensing systems to measure rotor blade structural dynamics,” *Mechanical Systems and Signal Processing*, Vol. 158, 107758, 2021.
11. Hajek, M., Manner S., and Susse, S., “Blade root integrated optical fiber Bragg grating sensors a highly redundant data source for future HUMS,” American Helicopter Society 71st Annual Forum Proceedings, Virginia Beach, Virginia, USA, May 2015.

12. Berghammer, F., Sosa, B., Heuschneider, V., Yavrucuk, I., "Testing of a Fiber-Optical Sensor System for Rotor Blade HUMS," Vertical Flight Society's 79th Annual Forum & Technology Display, West Palm Beach, Florida, USA, May 2023.

13. Serafini J., Bernardini, G., Mattioni, L., Vezzari V., and Ficuciello, C., "Non-invasive dynamic measurement of helicopter blades," *Journal of Physics*: Conference Series 882, 012014, 2017.

14. Weber, S., Southgate, D., Mullaney, K., James, S. W., Rutherford, R., Sharma, A., Lone, M., Kissinger, T., Chehura, E., Staines, S., Pekmezci, H., Fragonara, L. Z., Petrunin, I., Williams, D., Moulitsas, I., Cooke, A., Lawson, N., Rosales, W., Tatam, R. P., Morrish, P., Fairhurst, M., Atack, R., Bailey, G., Morley, S., "BLADESENSE – A novel approach for measuring dynamic helicopter rotor blade deformation," 44th European Rotorcraft Forum, Delft, The Netherlands, September 2018.

15. James, S. W., Kissinger, T., Weber, S., Mullaney, K., Chehura, E., Pekmezci, H. H., Barrington, J. H., Staines, S. E., Charrett, T. O. H., Lawson, N., Lone, M., Atack, R., and Tatam, R. P., "Fibre-optic measurement of strain and shape on a helicopter rotor blade during a ground run: 1. Measurement of strain," *Smart Materials & Structures*, Vol. 31, (7), 075014, 2022. DOI: 10.1088/1361-665X/ac736c.

16. James, S. W., Kissinger, T., Weber, S., Mullaney, K., Chehura, E., Pekmezci, H. H., Barrington, J. H., Staines, S. E., Charrett, T. O. H, Lawson, N., Lone, M., Atack, R., and Tatam, R. P., "Fibre-optic measurement of strain and shape on a helicopter rotor blade during a ground run: 2. Measurement of shape," *Smart Materials & Structures*, Vol. 31, (7), 075015, 2022. DOI: 10.1088/1361-665X/ac736c.

17. James, S. W., Kissinger, T., Weber, S., Mullaney, K., Chehura, E., Barrington, J. H., Pekmezci, H. H., Staines, S. E., Charrett, T. O. H, Lawson, N., Lone, M., and Tatam, R. P., "Dynamic Measurement of Strain and Shape on a Rotating Helicopter Rotor Blade: The Measurement Challenge," 28th International Conference on Optical Fiber Sensors, Hamamatsu, Japan, November 2023.

18. Zhang, H., Wang, Z., Teng, F., Xia, P., "Dynamic Strain Measurement of Rotor Blades in Helicopter Flight Using Fiber Bragg Grating Sensor," *Sensors*, Vol. 23, (15), 6692, 2023.

19. Copp, P., "Whole Span Rotorcraft Blade Structurally Embedded Elastic Deflection Including Twist (SEEDIT) Sensor", Vertical Flight Society, 6th Decennial Aeromechanics Specialists' Conference, Santa Clara, California, USA, February 2024.

20. Weber, S., Rammer, R., Camerini, V., Asselin, M., Kurfiss, F., Köhr, B., "Comparing FBG Sensors with Electrical Strain Gauges on a Helicopter Rotor Blade during Whirl Tower Test", European Test and Telemetry Conference, June, 2024.

21. Manzato, S., Grappasonni, C., Santopadre, C., Coppotelli, G., Peeters, B., Ameri, N., Ewins, D. J, "Dealing with harmonics and noise for advanced dynamic identification using in-flight helicopter data", IFASD International Forum of Aeroelasticity and Structural Dynamics, Bristol, United Kingdom, June 2013.

22. Manzato, S., White, J. R., LeBlanc, B., Peeters, B., Janssens, K., "Advanced identification techniques for operational wind turbine data", International Modal Analysis Conference IMAC, Los Angeles, United States, February 2013.

23. Peeters, B., Cornelis, B., Janssens, K., Van der Auweraer, H., "Removing Disturbing Harmonics in Operational Modal Analysis", Proceedings of IOMAC 2007, Copenhagen, Denmark, May 2007.

24. Manzato, S., Devriendt, C., Weijtjens, W., Di Lorenzo, E., Peeters, B., Guillaume, P., "Removing the influence of rotor harmonics for improved monitoring of offshore wind turbines", 32nd International Conference on Modal Analysis, IMAC-XXXII, Orlando, United States, February 2014.

25. Orlowitz, E., Brandt, A., "Comparison of experimental and operational modal analysis on a laboratory test plate", *Measurement*, Vol. 102, 2017, pp. 121-130. DOI: https://doi.org/10.1016/j.measurement.2017.02.001.

26. Grappasonni, C., Ameri, N., Coppotelli, G., Ewins, D. J., Colombo, A., Bianchi, E., Barraco,

V., "Dynamic identification of helicopter structures using operational modal analysis methods in the presence of harmonic loading", International Conference on Noise and Vibration Engineering, Leuven, Belgium, September 2012.

27. Herlufsen, H., Gade, S., Konstantin-Hansen, H., and Vold, H., "Characteristics of the Vold-Kalman order tracking filter," 2000 IEEE International Conference on Acoustics, Speech, and Signal Processing. Proceedings (Cat. No.00CH37100), Vol. 6, Istanbul, Turkey, 2000, pp. 3895-3898. DOI: 10.1109/ICASSP.2000.860254.

28. Vold, H., Mains, M., Blough, J., "Theoretical Foundations for High Performance Order Tracking with the Vold-Kalman Tracking Filter", *SAE* Technical Paper 972007, 1997. DOI: http://www.jstor.org/stable/44720079.

29. Manzato, S., Moccia, D., Peeters, B., Janssens, K., White, J. R., "A review of harmonic removal methods for improved operational modal analysis of wind turbines", In Proceedings of International Conference on Noise and Vibration Engineering, Vol. 4, Leuven, Belgium, September 2012, pp. 2675-2690.

30. Camerini, V., Coppotelli, G., Bendisch, S., Kiehn, D., "Impact of pulse time uncertainty on synchronous average: Statistical analysis and relevance to rotating machinery diagnosis", Mechanical Systems and Signal Processing, 2019, 129: 308-336.

31. Urbanek, J., Barszcz, T., Antoni, J., "A two-step procedure for estimation of instantaneous rotational speed with large fluctuations", *Mechanical Systems and Signal Processing*, Vol. 38, (1), 2013, pp. 96-102. DOI: https://doi.org/10.1016/j.ymssp.2012.05.009.

32. Kissinger, T., Correia, R., Charrett, T. O. H., James, S. W. and Tatam, R. P., "Fiber segment interferometry for dynamic strain measurements" *Journal of Lightwave Technology*, Vol. 34 (19) 4620–6, 2016.

33. Zahid, F. B., Ong, Z. C., and Khoo, S. Y., "A review of operational modal analysis techniques for in-service modal identification", *Journal of the Brazilian Society of Mechanical Sciences and Engineering*, Vol. 42, (8), 398, 2020.

34. Avitabile, P., *Modal Testing. A Practitioner's Guide, John* Wiley & Sons Ltd, Hoboken, NY, USA, 2018.

35. Padfield, G. D., *Helicopter Flight Dynamics. The Theory and Application of Flying Qualities and Simulation Modelling,* Blackwell Publishing, United Kingdom, second edition, 2007.

36. Van Overschee, P., De Moor, B., *Subspace Identification for Linear Systems: Theory and Implementation – Applications*, Kluwer Academic Press, Dordrecht, 1996.

37. Groover C. L., Trethewey M. W., Maynard K. P. and Lebold M. S., "Removal of order domain content in rotating equipment signals by double resampling", *Mechanical Systems and Signal Processing*, Vol. 19, (3), 483-500, 2005. DOI: https://doi.org/10.1016/j.ymssp.2003.09.008.

38. Mohaveny P., "Operational Modal Analysis in the Presence of Harmonic Excitation", PhD dissertation thesis, Technische Universiteit Delft, 2005.

39. Fyfe, K. R., and Munck, E. D. S., "Analysis of computed order tracking", *Mechanical systems and signal processing*, Vol. 11, (2), 187-205, 1997.

40. Blough, J., "Understanding the Kalman/Vold-Kalman Order Tracking Filters' Formulation and Behavior", SAE 2007 Noise and Vibration Conference and Exhibition, Cairns, Australia 2007. DOI: https://doi.org/10.4271/2007-01-2221.

41. Ewins, D. J., *Modal Testing – Theory, Practice and Application*, second ed., Research Studies Press Ltd., Exeter, Great Britain, 2000.

42. Boden, F., Maucher, C., "Blade Deformation Measurements with IPCT on an EC 135 Helicopter Rotor", *Advanced In-Flight Measurement Techniques*. Research Topics in Aerospace. Springer, Berlin, Heidelberg, Germany, 2013. DOI: https://doi.org/10.1007/978-3-642-34738-2_13.

43. Weber, S., "Fibre Optic Sensing for Measuring Rotor Blade Structural Dynamics", Ph.D Thesis, 2019.